Analytica Chimica Acta 1359 (2025) 344130

Contents lists available at ScienceDirect

Analytica Chimica Acta

journal homepage: www.elsevier.com/locate/aca

Tiny but mighty! *N,N*-dimethyl-4-(5-nitrothiophen-2-yl)aniline, a push-pull fluorescent dye for lipid droplet imaging

Wen Ann Wee [b,1], Tatum Melati Andini [c,1], Tomotaka Kumagai [a], Shanmugavel Chinnathambi [b], Ganesh N. Pandian [b], Arthur Millius [d], Hiroshi Sugiyama [b], Daron M. Standley [c], Soyoung Park [d,*]

[a] Department of Chemistry, Graduate School of Science, Kyoto University, Kitashirakawa-oiwakecho, Sakyo-ku, Kyoto, 606-8502, Japan
[b] Institute for Integrated Cell-Material Sciences (iCeMS), Kyoto University, Yoshida-ushinomiyacho, Sakyo-ku, Kyoto, 606-8501, Japan
[c] Department of Genome Informatics, Research Institute for Microbial Diseases, Osaka University, 3-1 Yamadaoka, Suita, 565-0871, Japan
[d] Laboratory of System Immunology, Immunology Frontier Research Center, Osaka University, Suita, Osaka, 565-0871, Japan

HIGHLIGHTS

- NiTA shows strong solvatochromism, with a ~160 nm red shift in fluorescence.
- NiTA selectively stains lipid droplets in cells, confirmed by colocalization studies.
- NiTA reveals increased lipid droplet formation under oxidative stress and starvation.
- In medaka embryos, NiTA tracks lipid dynamics, showing yolk and oil droplet changes.
- NiTA effectively visualizes cholesterol flux in HeLa and BJ cells.

GRAPHICAL ABSTRACT

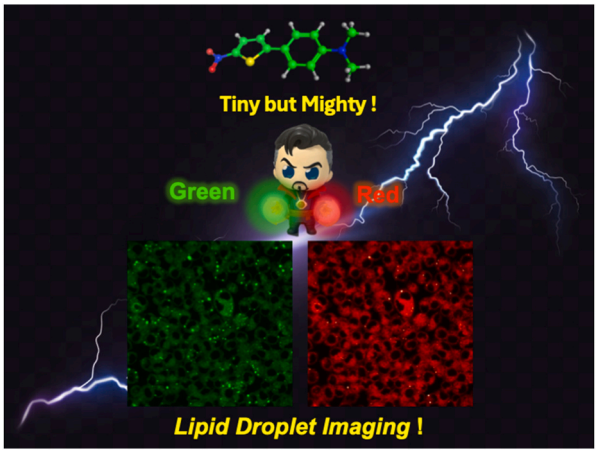

ARTICLE INFO

Handling Editor: Dr Jing-Juan Xu

Keywords:
Lipid droplets
LD probe
Fluorescent probe
Push-pull dye
Solvatochromism

ABSTRACT

Lipid droplets (LDs) are ubiquitous cellular organelles with a neutral lipid core containing triacylglycerols and cholesteryl esters surrounded by phospholipids. Recent findings indicate that LDs are intricately linked to diseases, such as cancer and neurological disorders, in addition to their roles in cellular senescence and immune responses. Herein, we describe a simple yet robust push-pull molecule, *N,N*-dimethyl-4-(5-nitrothiophen-2-yl) aniline (**NiTA**), as a versatile LD fluorescent probe. **NiTA** showed an absorption spectrum with a substantial bathochromic shift and a fluorescence spectrum with excellent solvatochromism. Leveraging the remarkable photophysical features of **NiTA**, we stained LDs in major immune cells, including T and B cells, and macrophages,

* Corresponding author.
E-mail address: spark@ifrec.osaka-u.ac.jp (S. Park).
[1] These authors contributed equally to this work.

https://doi.org/10.1016/j.aca.2025.344130
Received 14 January 2025; Received in revised form 1 April 2025; Accepted 27 April 2025
Available online 28 April 2025

and monitored the changes in LDs under oxidative and starvation conditions. Furthermore, we demonstrated the applicability of **NiTA** for visualizing the organization of medaka fish (*Oryzias latipes*) embryos during development. We expect the small yet powerful **NiTA** to be utilized in various applications, including fluorescence mapping to observe LD numbers, morphology, and polarity changes in animals and cells.

1. Introduction

Intramolecular charge transfer (ICT) molecules possess appealing qualities that have resulted in great interest in their application as environment-sensitive dyes [1–5]. These molecules are classified as push-pull dyes containing spatially separated yet chemically connected electron-donating and -withdrawing groups. Charge transfer from the donor to the acceptor moiety upon excitation generates the ICT species. In twisted intramolecular charge transfer (TICT) species, the charged ICT state is accessed through rotation of the bond connecting the donor and acceptor moieties and is typically formed in polar solvents [6]. In contrast, the planar intramolecular charge transfer (PICT) model postulates that an increased double bond character is formed between the donor and acceptor moieties [7,8]. Due to the opening of additional nonradiative relaxation pathways through the formation of the TICT state, conditions that favor the formation of TICT species often result in a decrease in quantum yield. ICT molecules are known for their environment-responsive properties because of the dependence of relaxation pathways on solvent properties, such as viscosity. Stabilizing the TICT state in polar environments also confers solvatochromic properties to such molecules, making them suitable as environment-sensitive dyes [9,10]. This is particularly evident in the utilization of ICT molecules for biological applications. For example, thioflavin T derivatives have been used to determine the fibril characteristics of neurological diseases, BODIPY derivatives have been employed in environmental pH imaging, and Nile Red has been extensively used to visualize cellular lipid droplets (LDs) [11–16].

LDs are highly conserved organelles in cells [17,18]. They have a hydrophobic core composed primarily of triacylglycerides and cholesteryl esters (CEs). Due to their ability to sequester lipids, they serve as energy stores and, crucially, buffers against high cellular fatty acid concentrations. The fatty acid-buffering capacity conferred by high LD numbers aids in mediating lipotoxicity and endoplasmic reticulum stress. Thus, dysfunctions in LD mechanisms have been associated with a range of diseases, including cancers, mitochondrial disorders, obesity, and diabetes [19]. Recent studies have revealed that LDs are essential hubs actively involved in antitumor immunity, anti-infective immunity, and metabolic disease [20–24]. Given the increasing significance of LD research and the remaining uncertainties and questions about the role of LDs, the demand for versatile LD probes is growing [37]. In this context, several LD dyes—including BODIPY, Lipi-Blue, and Nile Red—have been developed and widely utilized for LD imaging and analysis [25–36]. However, these conventional dyes exhibit notable limitations. For example, Nile Red shows poor solubility in aqueous environments, making it unsuitable for labeling biomolecules under physiological conditions [69]. While Lipi-Blue is effective for visualizing intracellular lipid content, it lacks sensitivity to changes in intracellular polarity. BODIPY dyes, though well known for their high brightness and photostability, often suffer from excessive lipophilicity. This property can lead to undesirable interactions with cell membranes, resulting in membrane penetration and accumulation within subcellular compartments. Furthermore, in polar environments such as the cytosol or extracellular space, BODIPY derivatives are prone to aggregation, which can induce aggregation-caused quenching (ACQ) and compromise fluorescence signal stability [70]. These issues limit the utility of conventional dyes in the dynamic imaging of lipid droplets and intracellular microenvironments. To overcome these challenges, it is crucial to develop LD probes that are not only photostable and highly specific, but also responsive to environmental polarity changes [71–74]. In particular, compact fluorescent probes that enhance cellular permeability while minimizing interference with native biomolecular interactions are highly desirable [38,39].

In pursuit of this goal, we have been actively developing fluorescent probes for monitoring biomolecular behavior. Specifically, we previously developed isomorphic fluorescent nucleobases that retain the native characteristics of natural nucleobases while exhibiting strong fluorescence [40–43]. More recently, we introduced a highly emissive, microenvironment-sensitive fluorogenic probe, $^{\mathbf{Thex}}\mathbf{T}$—a molecular rotor-containing thymidine nucleoside that fluoresces vividly upon interaction with target proteins [44]. $^{\mathbf{Thex}}\mathbf{T}$ features a compact structure, composed of thiophene and dimethylaniline moieties connected to a 5-iodouracil nucleoside via an olefinic bond, offering favorable photophysical properties. Inspired by the compact yet functionally rich structure of $^{\mathbf{Thex}}\mathbf{T}$, we sought to expand this design concept toward the development of a novel LD-specific probe. In this study, we report the design, synthesis, and characterization of *N,N*-dimethyl-4-(5-nitrothiophen-2-yl)aniline (**NiTA**), a push–pull type TICT fluorophore featuring a nitrothiophene acceptor and a dimethylaniline donor. The incorporation of a strong electron-withdrawing nitro group enhances the charge transfer characteristics of the dye, resulting in a red-shifted absorption spectrum and pronounced solvatochromism in the emission profile. Finally, we evaluated the applicability of **NiTA** in biological imaging by visualizing the structural organization and developmental progression of *Oryzias latipes* (medaka fish) embryos at various stages, demonstrating its practical potential as a versatile LD imaging probe.

2. Materials and methods

2.1. Synthesis

2-Bromo-5-nitrothiophene, (4-(dimethylamino)phenyl)boronic acid, triphenylphosphine, and sodium carbonate were obtained from FUJIFILM Wako Pure Chemical Corporation (Osaka, Japan) and used without further purification. Palladium(II) acetate was purchased from TCI (Portland, OR, USA) and used as received. All other chemicals and solvents were purchased from Sigma-Aldrich (St. Louis, MO, USA), FUJIFILM Wako Pure Chemical Corporation, TCI, and Kanto Chemical Co, Inc (Tokyo, Japan) and used without further purification. All reactions were performed under an argon atmosphere unless otherwise stated. Nuclear magnetic resonance (NMR) spectra were recorded using a JNM ECZ-600/S1 spectrometer (JEOL, Tokyo, Japan) operating at 600 MHz for ^{1}H NMR and 150 MHz for ^{13}C NMR in $CDCl_3$ unless otherwise noted. The detailed synthetic procedure and characterization of NiTA are provided in the Supporting Information.

2.2. Photophysical characterization

Fluorescence measurements were obtained using 3 mm path length JASCO FMM-100 quartz microcells on a JASCO FP-8300 Spectrofluorometer equipped with a JASCO EHC-573 temperature controller (JASCO Inc., Tokyo, Japan). The emission spectra were recorded as the average of two scans from 400 nm to 750 nm and at a scan rate of 1000 nm/min. The samples were excited for each solvent at the wavelength at which the maximum absorbance was observed. For aqueous samples, the excitation wavelength was set to 450 nm.

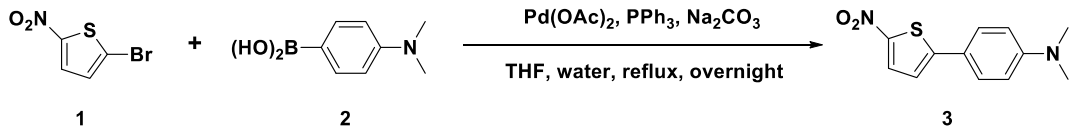

Scheme 1. Synthesis of *N,N*-dimethyl-4-(5-nitrothiophen-2-yl)aniline (NiTA).

2.3. Fluorescence imaging of LDs in various cells

For cellular LD staining, Jurkat, LK35.2, and Raw 264.7 cells were prepared at a concentration of 5×10^5 cells mL^{-1} in 1.5 mL sterile tubes. Cells were stained with the indicated concentrations of **NiTA** diluted in Dulbecco's modified Eagle's medium (DMEM)-HEPES (Gibco; Thermo Fisher Scientific, Waltham, MA, USA) with 2 % fetal bovine serum (FBS, Gibco; Thermo Fisher Scientific) and incubated at 37 °C under 5 % CO_2 for 30 min. After staining, the cells were washed after staining with (D)-phosphate-buffered saline (Gibco; Thermo Fisher Scientific) and added to DMEM, high glucose, HEPES, no phenol red (DMEM HEPES, Gibco; Thermo Fisher Scientific), and 2 % FBS (Gibco; Thermo Fisher Scientific). Next, the cells were resuspended and transferred to well slides (μ-slide 8 Well ibiTreat; Ibidi, Gräfelfing, Germany) for further observation using confocal microscopy (FV 3000; Olympus Corporation, Tokyo, Japan). The fluorescence detection included excitation at 488 nm and an emission wavelength of 480–560 nm for the green channel and an emission wavelength of 620–720 nm for the red channel. Subsequently, the images were processed using ImageJ software (National Institutes of Health, Bethesda, MD, USA).

2.4. Medaka fish embryo imaging

In vivo staining was conducted using medaka fish embryos. Mature medaka fish were obtained from a local fish farm and kept in a freshwater aquarium maintained at 25 °C with a 10-h dark and 14-h light cycle. After spawning, the eggs were collected and monitored in a Petri dish. On day 4, the eggs were seeded individually in triplicate in a 96-well plate. After **NiTA** treatment (300 nM, starting 3 days post-fertilization), the eggs were monitored for 32 days. The hatched larvae were placed in separate tanks for monitoring. ImageJ software was used to calculate the average fluorescence intensities of medaka fish embryos and larvae.

3. Results and discussion

3.1. Synthesis and photophysical properties

We developed a compact push-pull-type fluorescent dye by combining dimethylaniline as the electron donor moiety and 2-nitrothiophene as the electron acceptor moiety. **NiTA** was synthesized by Suzuki–Miyaura cross-coupling between 2-bromo-5-nitrothiophene and 4-(dimethylamino)phenylboronic acid under optimized conditions based on literature (Scheme 1) [68]. The synthesized compound was characterized using ^{1}H NMR, ^{13}C NMR, and ESI-MS, as detailed in the Supporting Information.

We also synthesized several **NiTA** derivatives with various combinations of donor and acceptor moieties (see Supplementary Information

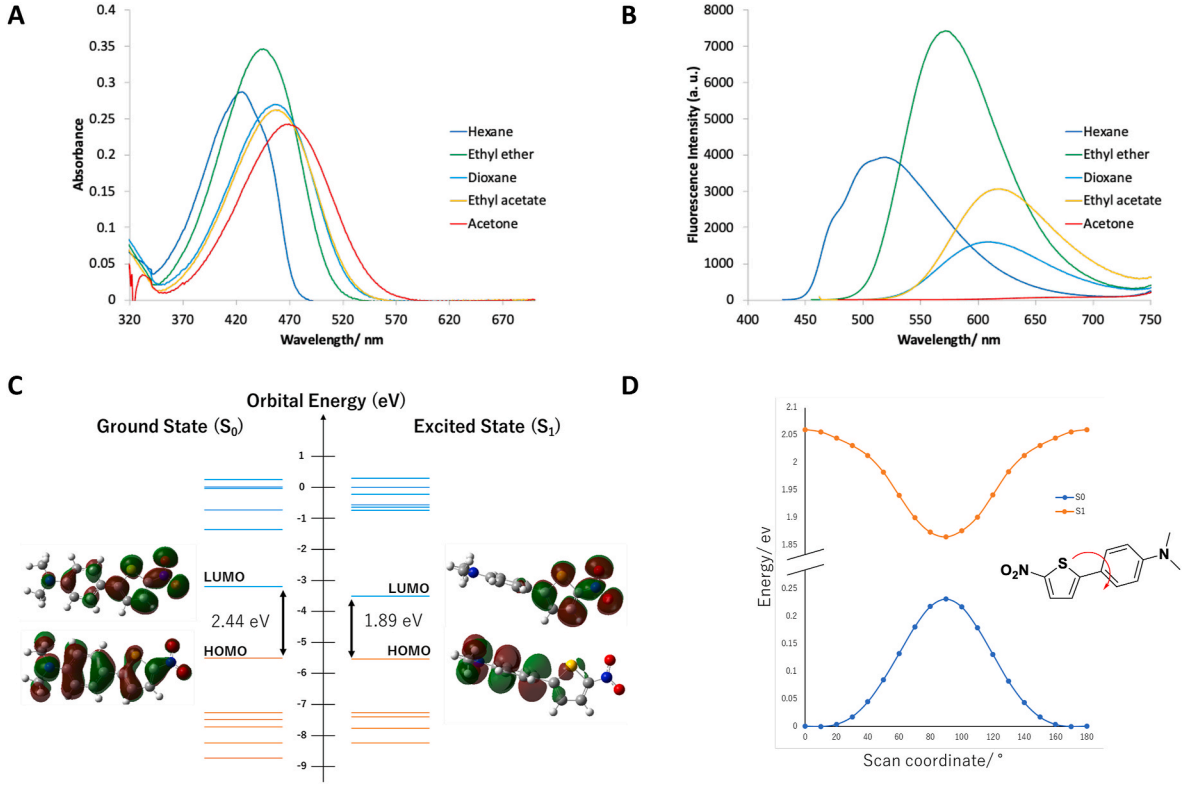

Fig. 1. Photophysical characterization of NiTA. (A) Absorption and (B) Fluorescence spectra of NiTA in different solvents. (C) HOMO-LUMO levels and electron distributions of NiTA. (D) Dihedral coordination scan results of NiTA at S_0 (blue line) and S_1 (orange line) states (0−180°). The results depicted in (C) and (D) were obtained from TD-DFT calculations performed at the B3LYP/6-311+G(d,2p) level. (For interpretation of the references to color in this figure legend, the reader is referred to the Web version of this article.)

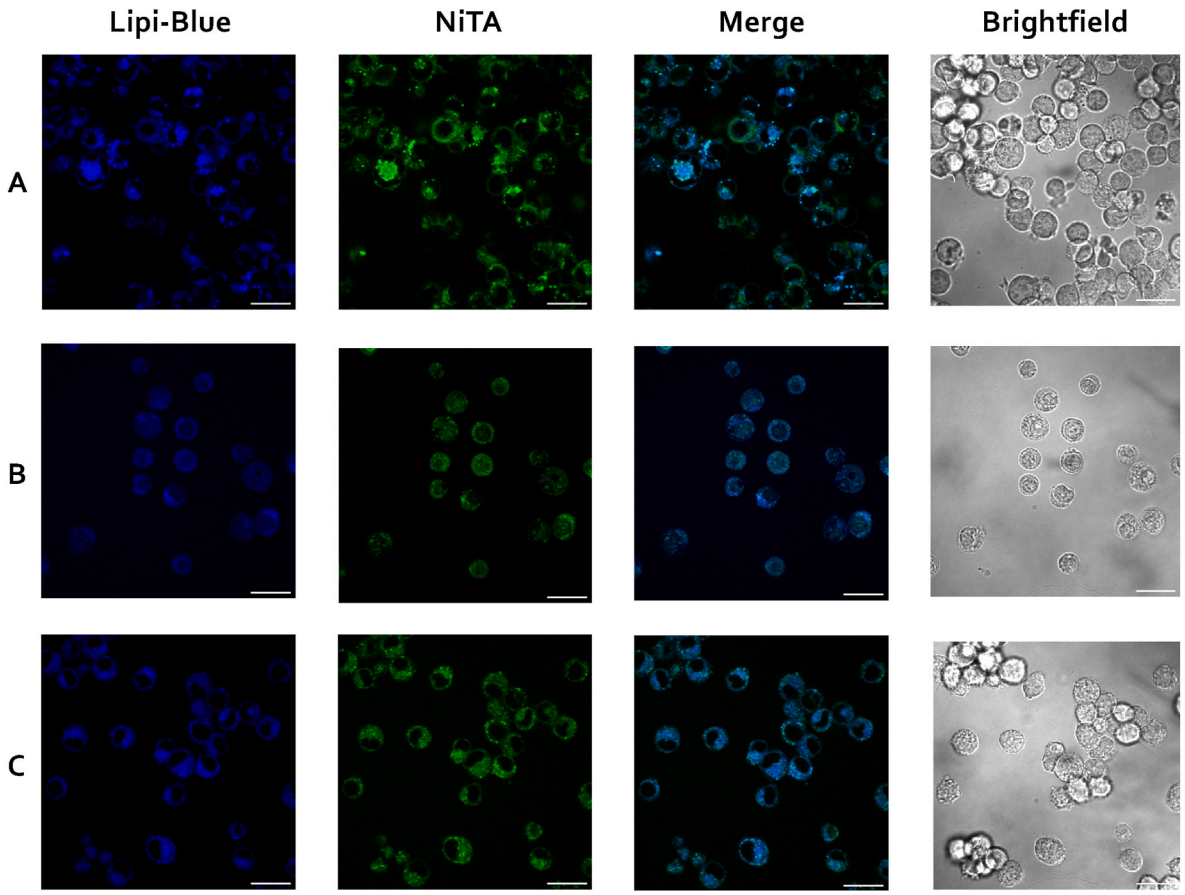

Fig. 2. Live-cell imaging with co-staining of Lipi-Blue and **NiTA** demonstrates the colocalization of lipid droplets in different cell types. The Pearson correlation coefficient confirms the ability of **NiTA** to target lipid droplets, with the following results: (A) Jurkat cells: r = 0.79; (B) LK35.2 cells: r = 0.83; (C) RAW 264.7 cells: r = 0.95. Jurkat and LK35.2 cells were treated with **NiTA** at a concentration of 2.5 μM, while RAW 264.7 cells were treated with **NiTA** at 300 nM concentration. All cells were co-stained with Lipi-Blue (1 μM) and incubated for 30 min. Images were acquired using an excitation wavelength of 405 nm and emission 400–470 nm for Lipi-Blue, and excitation 488 nm with emission 480–560 nm for the **NiTA** green channel. Scale bar: 20 μm. (For interpretation of the references to color in this figure legend, the reader is referred to the Web version of this article.)

for details). All derivatives were synthesized using the same method as that for **NiTA** and were obtained at moderate to high yields. **AcTA**, which employs an acetyl group instead of a nitro group, exhibits higher quantum yields and a better fluorescence response to solvent polarity than **NiTA**. However, it has a shorter emission wavelength and a narrower range of absorption wavelengths. **NiTM**, which contains a methoxy group instead of a dimethylamino group, and **NiFA**, which uses furan instead of thiophene, both exhibited lower fluorescence intensities (Fig. S1, Table S1–S4 and Fig. S6). Consequently, we adopted **NiTA** in this study. UV–visible spectroscopy revealed the apparent extent of the bathochromic shift in the absorption spectra of **NiTA** with increasing solvent polarity (Fig. 1A). With an increase in the solvent polarity from nonpolar hexane to polar acetone, the absorption spectra shifted from 426 to 469 nm. Fluorescence spectroscopy showed that **NiTA** demonstrated remarkable solvatochromism (157 nm shift) when dissolved in various solvents. It emitted fluorescence with red-shifted emission from 518 nm in nonpolar hexane to 675 nm in polar acetone (Fig. 1B). The structural and photophysical characteristics of **NiTA** suggest that it likely undergoes ICT upon excitation. The outcome of ICT varies depending on whether the ICT state is twisted (TICT) or planar (PICT). TICT is typically characterized by red-shifted emissions with low quantum yields in polar solvents. In contrast, although PICT can result in strong Stokes shifts in nonpolar solvents, emissions from the PICT state tend to have higher quantum yields. The increasing red-shift and reduction in the quantum yield of **NiTA** with increasing solvent polarity are thus consistent with an increasingly favored transition toward TICT emission. To clarify its behavior in the excited state, we performed density functional theory calculations, including the energy levels and electron densities in three representative solvents, as well as the most stable structure of **NiTA** in the ground and excited states. The energy gap between the highest occupied molecular orbital (HOMO) and the lowest unoccupied molecular orbital (LUMO) corresponds to the photon energy absorbed or emitted by the compounds (Fig. 1C). These gaps gradually decrease with increasing solvent polarity in both the ground and excited states (Fig. S2). This indicates that the absorption and fluorescence wavelengths increased as solvent polarity increased, consistent with the experimental results. In addition, electrons are localized in different moieties between the HOMO and LUMO, indicating that **NiTA** acts as a D-A type molecule. The computational results also support the idea that **NiTA** forms a TICT state under light irradiation (Fig. 1D and Figure S3).

3.2. *NiTA stains LDs in various cells*

To utilize the remarkable photophysical characteristics of **NiTA** for imaging LDs, we first verified whether **NiTA** could selectively stain LDs. Since **NiTA** has a broad emission range from green to red wavelengths, we chose the LD-specific dye Lipi-Blue which has an absorption wavelength of approximately 405 nm and an emission band from 400 to 470 nm, as a co-stain [33]. Confocal imaging of Jurkat, LK35.2, and RAW 264.7 cells co-stained with both **NiTA** using 2.5 μM for Jurkat and LK35.2, while Raw 264.7 using 300 nM concentration and Lipi-Blue 1 μM concentration confirmed that the signals from **NiTA** and Lipi-Blue

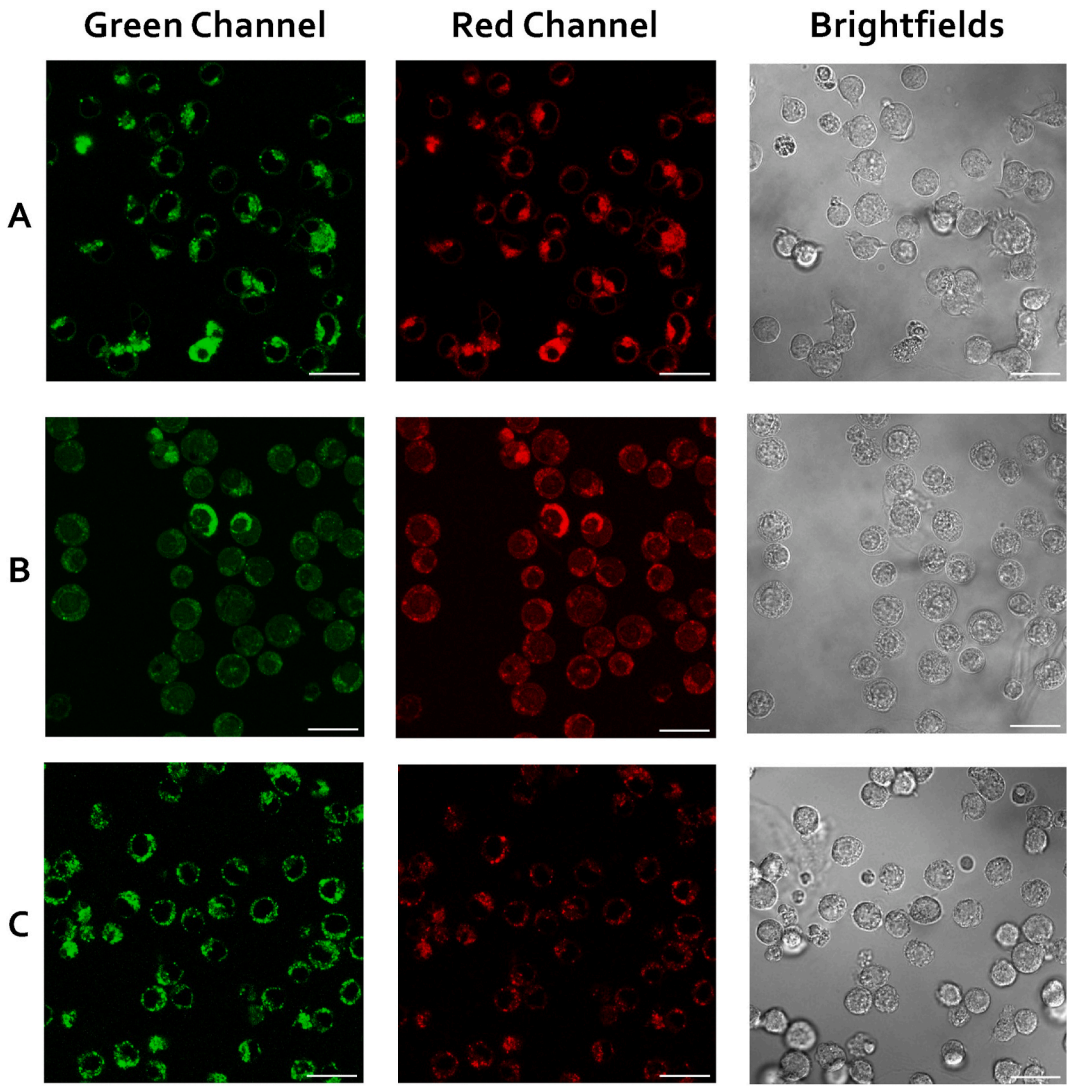

Fig. 3. Live-cell imaging of immune cell lines: (A) T cells (Jurkat cells), (B) B cells (LK35.2 cells), and (C) macrophages (RAW 264.7 cells). Jurkat and LK35.2 cells were treated with **NiTA** at a concentration of 2.5 μM, while RAW 264.7 cells were treated with **NiTA** at 300 nM concentration, and cells were incubated for 30 min. Images were obtained at an excitation of 488 nm with 480–560 nm for the green channel and 620–720 nm for the red channel. Each cell type exhibits varying fluorescence intensities across the different channels. Scale bar: 20 μm. (For interpretation of the references to color in this figure legend, the reader is referred to the Web version of this article.)

colocalized with each other, indicating that **NiTA** selectively stained LDs (Fig. 2). As depicted in Fig. 2, the Pearson correlation coefficients (r) between **NiTA** and Lipi-Blue were calculated to quantify the degree of spatial colocalization. The results demonstrated high correlation values: Jurkat cells, $r = 0.79$; LK35.2 cells, $r = 0.83$; RAW 264.7 cells, $r = 0.95$. These values indicate excellent spatial overlap between the two dyes, further supporting the specificity of **NiTA** for LD staining. The robust co-localization with Lipi-Blue validates the usability of **NiTA** as a reliable probe for LDs in diverse cell types (Figs. S4 and S5). This selectivity can be attributed, in part, to the turn-on fluorescence exhibited by **NiTA** in a low-polarity environment. As the intracellular environment is generally aqueous, the inherently hydrophobic interior of lipid droplets ensures that the emission of **NiTA** within the LDs is higher than that outside. Cell viability assays were conducted to determine the suitability of **NiTA** as a stain for live-cell imaging (Fig. S7). Cell viability was not affected following treatment with up to 50-fold the normal treatment concentration.

Immune cells are involved in the development and progression of many diseases, including cancer, neurological disorders, and infectious and autoimmune diseases. Recently, LDs in immune cells have gained significant interest because they not only regulate homeostasis through the storage and degradation of neutral lipids but also directly intertwine with various immune responses [45,46]. Marschallinger and colleagues reported that LD accumulation in microglia induces the secretion of pro-inflammatory cytokines and contributes to neurodegeneration associated with aging [47]. LDs reportedly play an important role in antiviral responses by enhancing interferon production and suppressing viral replication [48,49]. These studies suggest that LDs are more than just fat depots in the immune system; as lipid mediators, they play a pivotal role in protecting the host from viral infection and are deeply involved in various diseases. Highly sensitive and non-destructive fluorescent probes are needed to stain and track LDs in immune cells to elucidate their role in various immune pathways and understand the underlying molecular mechanisms [50]. Encoraged by the effective and selective staining of LDs by NiTA in various immune cell types Fig. 2, we further investigated its dual emission fluorescence properties for LD monitoring in immune cells [66,67]. Upon 488 nm excitation, confocal imaging of T cells, B cells, and macrophages was performed using the green (480–560 nm) and red (620–720 nm) channels to evaluate **NiTA**'s fluorescence characteristics in these cells. Target cells were treated with

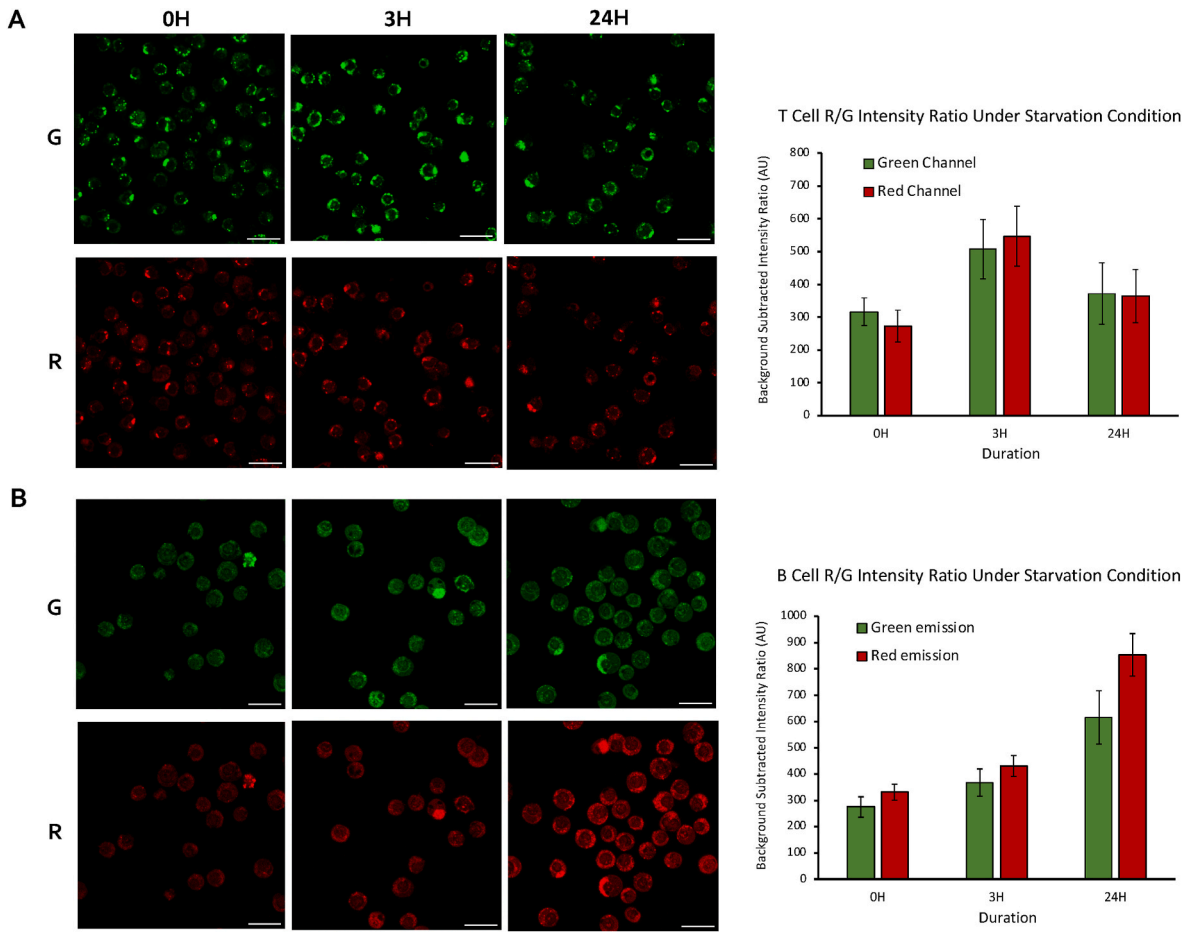

Fig. 4. Cell imaging and R/G intensity ratio of (A) T cells and (B) B cells under starvation conditions. Live imaging results were captured for both the green and red channels. Cell samples were treated using DMEM low glucose for 0 h, 3 h, and 24 h, then stained with **NiTA** 2.5 μM concentration for 30mins before the results taken with confocal microscopy imaging at 0 h as a control, and subsequently, after 3 h and 24 h to monitor the fluorescence intensity changes. Images were obtained at an excitation of 488 nm with 480–560 nm for the green channel and 620–720 nm for the red channel. Scale bar: 20 μm. n = 3. (For interpretation of the references to color in this figure legend, the reader is referred to the Web version of this article.)

2.5 μM **NiTA** as a working concentration for T and B cells and 300 nM for macrophages. After a brief incubation period, **NiTA** rapidly permeated the cellular membrane, exhibiting pronounced and intense fluorescence that distinctly labeled intracellular LDs (Fig. 3). The clear and vivid staining underscores the efficient and rapid performance of **NiTA** on LDs, affirming its ability to brightly and specifically illuminate lipid-rich structures within the cellular framework. To confirm the performance of **NiTA** as an LD-staining probe, we performed lipid extraction experiments using T and B cells and macrophages and found that **NiTA** clearly stained the extracted lipids (Fig. S8). In addition, we generated an artificial lipid-mimetic system using dioleoylphosphatidylcholine (DOPC), sphingomyelin, and cholesterol ester and found that **NiTA** readily labeled lipid vesicles with bright green and red fluorescence (Fig. S9). These observations substantiate the remarkable capacity of **NiTA** to achieve highly intensive LD staining, highlighting its potential as a robust fluorescent probe for lipid-related investigations and applications.

3.3. LD staining in immune cells under oxidative stress and starvation conditions

LDs serve a variety of cellular functions, including maintaining cellular lipid homeostasis by modulating toxicity in response to stressful conditions. LDs act as safeguards for lipid metabolism, effectively buffering toxic lipids or controlling the release of surplus lipids in response to various types of cellular stress. To monitor LDs in altered cellular environments, we conducted experiments under both starvation and oxidative stress conditions [51,52]. Hydrogen peroxide (H_2O_2) is a type of intracellular reactive oxygen species (ROS). To simulate ROS-induced oxidative stress conditions, T and B cells were stained with 2.5 μM **NiTA**, followed by treatment with 4 mM H_2O_2 for 1 h. Fluorescence imaging of both untreated and H_2O_2-treated cells revealed significant changes in fluorescence signals in both the green and red channels (Fig. S10). In H_2O_2-treated cells, an overall increase in fluorescence intensity was observed in both T and B cells, indicating an increase in LDs. This finding suggests that LDs accumulate in response to H_2O_2-induced oxidative stress, likely to sequester toxic lipids from peroxidation reactions and mitigate cellular damage. To further analyse these changes, we calculated the R/G fluorescence ratio for untreated and H_2O_2-treated cells. In T cells, the R/G fluorescence ratio increased significantly from 0.68 (untreated) to 0.89 (treated). In contrast, in B cells, the R/G fluorescence ratio showed a slight decrease from 1.03 (untreated) to 0.94 (treated). These differential responses likely stem from differences in lipid composition between the two cell types. Previous studies have shown that T cells contain higher cholesterol levels than B cells. Therefore, the observed increase in the R/G fluorescence ratio in T cells may be attributed to cholesterol peroxidation under oxidative stress conditions [53,54]. The dual-channel fluorescence signals observed with **NiTA** can be attributed to its environment-sensitive emission band that extends across both the green and red detection channels. Owing to its solvatochromic nature, **NiTA**'s emission maximum shifts in response to local polarity changes. Consequently, the R/G fluorescence ratio reflects

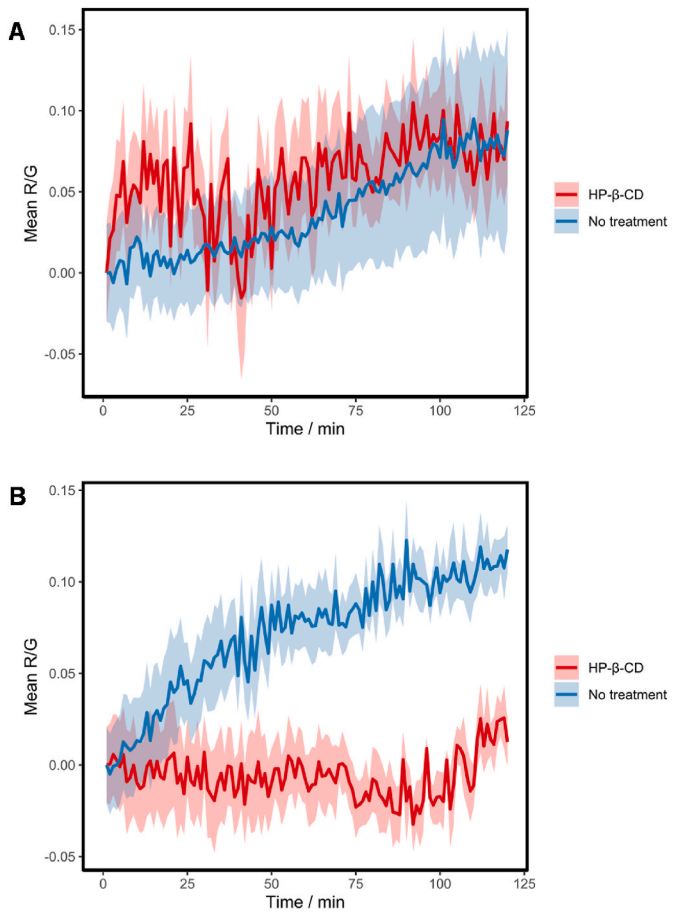

Fig. 5. Tracking changes in cellular cholesterol content using **NiTA**. Time-lapse imaging of (A) HeLa and (B) BJ cells in the presence of 1 mM hydroxypropyl-β-cyclodextrin (HPCD) in serum supplemented medium. Images were captured from 0, 25, 50, 75, 100, and 125 min.

polarity-induced redistribution of emission intensity rather than the presence of multiple discrete emission peaks. This behaviour is consistent with that of previously reported solvatochromic probes used for polarity mapping in live cells [66,67]. Taken together, the observed shifts in the R/G ratio are consistent with known effects of cholesteryl ester peroxidation under oxidative stress and underscore **NiTA**'s capability to sensitively report on microenvironmental polarity changes within lipid droplets.

We also conducted a separate set of experiments to monitor LD dynamics under starvation conditions. T and B cells were cultured in low-glucose, serum-free medium, and LDs were visualized using **NiTA** (Fig. 4). Under starvation, fluorescence intensity increased in both cell types, indicating enhanced LD formation. This is consistent with the cellular metabolic shift from glycolysis to mitochondrial fatty acid oxidation under nutrient deprivation, wherein lipids serve as alternative energy sources. To support this metabolic adaptation, cells increase LD formation to facilitate lipid storage and mobilization. Additionally, β-oxidation of lipids is upregulated during starvation, which can alter LD polarity. Previous studies have also reported increased cholesterol levels in adipose tissue during starvation [55]. Interestingly, the changes in the R/G fluorescence ratio during starvation exhibited distinct patterns between T and B cells. When LD imaging was tracked over time (3 h and 24 h of starvation), T cells displayed moderate fluctuations in the R/G fluorescence ratio: 0.87 (untreated), 1.08 (3 h), and 0.98 (24 h). Although the fluorescence intensity in both the green and red channels initially increased, the R/G ratio subsequently decreased, suggesting that T cells adapt to starvation conditions in a relatively stable manner. In contrast, B cells exhibited a steeper increase in fluorescence intensity and a more pronounced change in the R/G fluorescence ratio: 1.20 (untreated), 1.17 (3 h), and 1.37 (24 h). This trend suggests that B cells are more sensitive to nutrient stress. Cumulatively, these findings demonstrate that **NiTA** is a useful tool for monitoring LD dynamics in immune cells under stress conditions, such as oxidative stress and nutrient deprivation. Furthermore, our results highlight the differential susceptibility of T and B cells to such stressors, potentially linked to their distinct lipid compositions and metabolic adaptations.

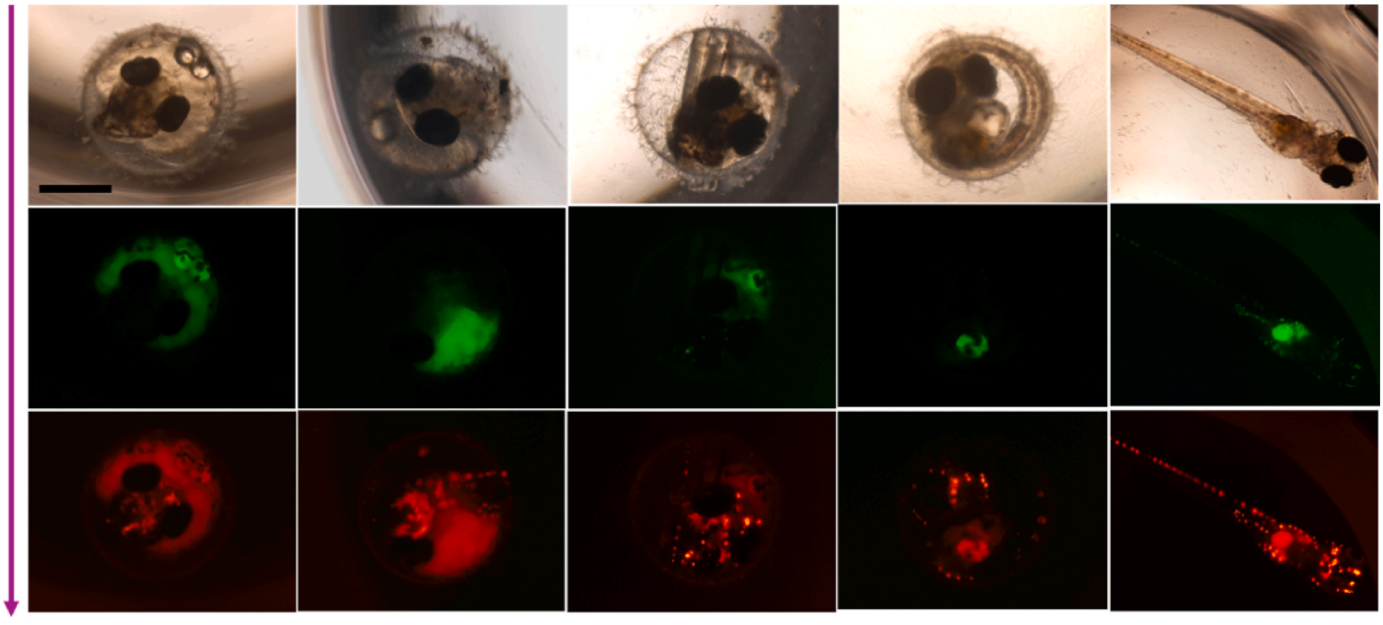

Fig. 6. Two-color confocal imaging of a medaka fish embryo (3 days post-fertilization) stained with 300 nM **NiTA**. Images were captured at 5, 9, 16, 25, and 32 days (left to right). Emission was detected in the green and red channels. (For interpretation of the references to color in this figure legend, the reader is referred to the Web version of this article.)

3.4. Cholesterol flux visualized by **NiTA**

The impressive LD staining performance of **NiTA** in altered cellular environments prompted us to explore its further applications. We envisioned that **NiTA** would enable the monitoring of the behavior of CEs associated with LDs in live cells [56–60]. To this end, we tracked the R/G ratio of **NiTA** in LDs over a period of 2 h in both HeLa and BJ cells. Cancer cells are reportedly enriched in LDs that enable stress minimization and tumor progression. HeLa cells are derived from cervical carcinoma cells, while BJ cells are fibroblasts obtained from normal foreskin tissue. Therefore, unlike BJ cells, HeLa cells are expected to exhibit cancer-like characteristics. To perturb CE levels in these cells, they were treated with hydroxypropyl-β-cyclodextrin (HPCD) in a serum-containing medium. HPCD acts as a cholesterol shuttle by encapsulating relatively hydrophobic cholesterol molecules within the cyclodextrin moiety, essentially coating the molecule with a hydrophilic shield. Including serum ensures that instead of depleting the cells of cholesterol, the intracellular cholesterol concentration would gradually equilibrate with that in the surrounding medium. By tracking live cells in real-time, we observed the equilibration of intra- and extracellular cholesterol.

Unexpectedly, live imaging of HeLa cells revealed no significant difference in the mean R/G between cells treated with HPCD and untreated cells (Fig. 5A). In contrast, the mean R/G ratio increased over time in untreated BJ cells but not in BJ cells treated with HPCD (Fig. 5B). These results suggested that, unlike BJ cells, no net inflow of cholesterol or CE into HeLa cells was observed; thus, compared with BJ cells, HeLa cells had higher cellular cholesterol or CE content. Consistent with these observations, LD accumulation has been implicated in cancer development. The dysregulation of cholesterol homeostasis has been increasingly associated with adverse cancer outcomes. Therefore, using **NiTA** as a ratiometric dye for cholesterol moieties could serve as a valuable tool for visualizing LD composition in live cells.

3.5. Medaka fish embryo imaging

Medaka fish embryos are versatile model organisms for studying various physiological and developmental processes that occur in a sophisticated manner in living organisms. Their transparent developmental stages allow for tractable *in vivo* imaging, eliminating the need to fix the target subject. This model is remarkable for investigating the effects of various biologically active molecules on developmental processes such as heart development and nervous system and bone formation [61–65]. For biocompatible visualization of fish eggs, we applied **NiTA** to medaka fish embryos to track oil droplets, yolk, and associated lipid content localized in medaka eggs. Our probe exhibited good permeability in medaka fish eggs, enabling the observation of the developmental stages of medaka fish embryos without requiring additional procedures following initial staining. As shown in Fig. 6, we observed a remarkable two-color imaging of **NiTA**, indicating the presence of yolk and oil droplets. We found that the volumes of the yolk and oil droplets declined significantly from 8 to 13 days post-fertilization. Owing to its stability in live cells, it forms lipid globules in the bodies of fish larvae after hatching. In fertilized medaka fish eggs, oil droplets can function as energy reservoirs for embryonic development and organogenesis. Yolk also contains large amounts of lipids and proteins. During maturation, the size of the yolk decreases because of the consumption of lipid contents such as phospholipids, triglycerides, and CEs for further development. Our results indicated the morphological changes in lipid-containing organelles as the fish embryos developed. The present study demonstrates the potential of **NiTA** for longitudinal studies of LD dynamics *in vivo*.

4. Conclusion

In conclusion, we developed a novel push-pull molecular rotor dye as a solvatochromic LD-targeting fluorescent probe, **NiTA**, that can stain intracellular LDs capably with low cytotoxicity and high biocompatibility. **NiTA** successfully detected LDs across various cell types, including cancer and immune cells, including T and B cells and macrophages. We monitored the alterations in LDs, including local polarity, under oxidative stress and starvation conditions. By applying **NiTA** to the cells, we tracked the changes in cholesterol content in both cancerous HeLa and non-cancerous BJ cells, highlighting these differences. Because changes in cellular cholesterol content are significant in many metabolic diseases, **NiTA** may serve as a valuable tool for visualizing these cell states in the future. Furthermore, we demonstrated the applicability of **NiTA** for visualizing lipid-rich organelles in medaka fish embryos and tracking their developmental stages. We anticipate that tiny, but mighty **NiTA** will be used for various applications such as fluorescence mapping to monitor LD numbers, morphology, and polarity changes at the animal level, as well as in cells. Beyond its imaging capabilities, **NiTA**'s minimal molecular structure and remarkable photophysical properties make it a promising scaffold for the development of miniaturized optical tags (200–300 Da). Its compact architecture allows for potential conjugation to various biomolecules, enabling multiplexed and targeted applications in biological imaging. Further studies to develop multifunctional LD-targeting probes based on the tunable features of push-pull dyes are currently underway in our laboratory.

CRediT authorship contribution statement

Wen Ann Wee: Writing – original draft, Visualization, Validation, Methodology, Investigation, Conceptualization. **Tatum Melati Andini:** Writing – original draft, Visualization, Validation, Investigation, Data curation. **Tomotaka Kumagai:** Validation, Software, Data curation. **Shanmugavel Chinnathambi:** Visualization, Validation. **Ganesh N. Pandian:** Visualization, Validation. **Arthur Millius:** Writing – review & editing, Validation. **Hiroshi Sugiyama:** Writing – review & editing, Supervision, Resources. **Daron M. Standley:** Writing – review & editing, Supervision, Resources. **Soyoung Park:** Writing – review & editing, Writing – original draft, Supervision, Resources, Project administration, Methodology, Funding acquisition, Conceptualization.

Declaration of competing interest

The authors declare that they have no known competing financial interests or personal relationships that could have appeared to influence the work reported in this paper.

Acknowledgement

We thank Karin Nishimura (Graduate School of Engineering, Kyoto University) for technical assistance in obtaining the mass spectra of the synthesized compounds. S.P. would like to acknowledge the "Rising Fellow Program" from Toyota Physical and Chemical Research Institute. This work was also supported by the Platform Project for Supporting Drug Discovery and Life Science Research (Basis for Supporting Innovative Drug Discovery and Life Science Research (BINDS)) from AMED (grant number: 22ama121025j0002) and the Japan Society for the Promotion of Science (Grant-in-Aid for Transformative Research Areas (A) "Biophysical Chemistry for Material Symbiosis" [grant number: 23H04076], Grant-in-Aid for Scientific Research (C) [grant number: 23K04961]) to S.P.

Appendix A. Supplementary data

Supplementary data to this article can be found online at https://doi.org/10.1016/j.aca.2025.344130.

Data availability

Data will be made available on request.

References

[1] D. Liese, G. Haberhauer, Rotations in excited ICT states – fluorescence and its microenvironmental sensitivity, Isr. J. Chem. 58 (2018) 813–826, https://doi.org/10.1002/ijch.201800032.

[2] M.A. Haidekker, E.A. Theodorakis, Environment-sensitive behavior of fluorescent molecular rotors, J. Biol. Eng. 4 (2010) 11, https://doi.org/10.1186/1754-1611-4-11.

[3] M.A. Haidekker, E.A. Theodorakis, Ratiometric mechanosensitive fluorescent dyes: design and applications, J. Mater. Chem. C Mater 4 (2016) 2707–2718, https://doi.org/10.1039/C5TC03504J.

[4] S.-C. Lee, J. Heo, H.C. Woo, J.-A. Lee, Y.H. Seo, C.-L. Lee, S. Kim, O.-P. Kwon, Fluorescent molecular rotors for viscosity sensors, Chemistry 24 (2018) 13706–13718, https://doi.org/10.1002/chem.201801389.

[5] A. Vyšniauskas, M.K. Kuimova, A twisted tale: measuring viscosity and temperature of microenvironments using molecular rotors, Int. Rev. Phys. Chem. 37 (2018) 259–285, https://doi.org/10.1080/0144235X.2018.1510461.

[6] S. Sasaki, G.P.C. Drummen, G. Konishi, Recent advances in twisted intramolecular charge transfer (TICT) fluorescence and related phenomena in materials chemistry, J. Mater. Chem. C 4 (2016) 2731–2743, https://doi.org/10.1039/C5TC03933A.

[7] C.A. Guido, B. Mennucci, D. Jacquemin, C. Adamo, Planar vs. twisted intramolecular charge transfer mechanism in nile red: new hints from theory, Phys. Chem. Chem. Phys. 12 (2010) 8016–8023, https://doi.org/10.1039/b927489h.

[8] C. Zhong, The driving forces for twisted or planar intramolecular charge transfer, Phys. Chem. Chem. Phys. 17 (2015) 9248–9257, https://doi.org/10.1039/c4cp02381a.

[9] A.S. Klymchenko, Solvatochromic and fluorogenic dyes as environment-sensitive probes: design and biological applications, Acc. Chem. Res. 50 (2017) 366–375, https://doi.org/10.1021/acs.accounts.6b00517.

[10] X. Qin, X. Yang, L. Du, M. Li, Polarity-based fluorescence probes: properties and applications, RSC Med. Chem. 12 (2021) 1826–1838, https://doi.org/10.1039/d1md00170a.

[11] D.R. Rogers, Screening for amyloid with the thioflavin T fluorescent method, Am. J. Clin. Pathol. 44 (1965) 59–61, https://doi.org/10.1093/ajcp/44.1.59.

[12] D.L. Sackett, J. Wolff, Nile red as a polarity-sensitive fluorescent probe of hydrophobic protein surfaces, Anal. Biochem. 167 (1987) 228–234, https://doi.org/10.1016/0003-2697(87)90157-6.

[13] C. Xue, T.Y. Lin, D. Chang, Z. Guo, Thioflavin T as an amyloid dye: fibril quantification, optimal concentration and effect on aggregation, R. Soc. Open Sci. 4 (2017) 160696, https://doi.org/10.1098/rsos.160696.

[14] F.Y. Yeasmin Khusbu, X. Zhou, H. Chen, C. Ma, K. Wang, Thioflavin T as a fluorescence probe for biosensing applications, Trends Analyt. Chem. 109 (2018) 1–18, https://doi.org/10.1016/j.trac.2018.09.013.

[15] X. Liu, W. Chi, Q. Qiao, S.V. Kokate, E.P. Cabrera, Z. Xu, X. Liu, Y.-T. Chang, Molecular mechanism of viscosity sensitivity in BODIPY rotors and application to motion-based fluorescent sensors, ACS Sens. 5 (2020) 731–739, https://doi.org/10.1021/acssensors.9b01951.

[16] S. Verma, V. Ravichandiran, N. Ranjan, Beyond amyloid proteins: thioflavin T in nucleic acid recognition, Biochimie 190 (2021) 111–123, https://doi.org/10.1016/j.biochi.2021.06.003.

[17] T. Fujimoto, R.G. Parton, Not just fat: the structure and function of the lipid droplet, Cold Spring Harbor Perspect. Biol. 3 (2011) a004838, https://doi.org/10.1101/cshperspect.a004838.

[18] A. Zadoorian, X. Du, H. Yang, Lipid droplet biogenesis and functions in health and disease, Nat. Rev. Endocrinol. 19 (2023) 443–459, https://doi.org/10.1038/s41574-023-00845-0.

[19] P. Shyu, X.F.A. Wong, K. Crasta, G. Thibault, Dropping in on lipid droplets: insights into cellular stress and cancer, Biosci. Rep. 38 (2018) 20180764, https://doi.org/10.1042/BSR20180764.

[20] P. Anand, S. Cermelli, Z. Li, A. Kassan, M. Bosch, R. Sigua, L. Huang, A.J. Ouellette, A. Pol, M.A. Welte, S.P. Gross, A novel role for lipid droplets in the organismal antibacterial response, Elife 1 (2012) e00003, https://doi.org/10.7554/eLife.00003.

[21] B.-R. Bang, M. Li, K.-N. Tsai, H. Aoyagi, S.-A. Lee, K. Machida, H. Aizaki, J.U. Jung, J.J. Ou, T. Saito, Regulation of hepatitis C virus infection by cellular retinoic acid binding proteins through the modulation of lipid droplet abundance, J. Virol. 93 (2019), https://doi.org/10.1128/JVI.02302-18.

[22] G. Bannenberg, C.N. Serhan, Specialized pro-resolving lipid mediators in the inflammatory response: an update, Biochim. Biophys. Acta 1801 (2010) 1260–1273, https://doi.org/10.1016/j.bbalip.2010.08.002.

[23] G. Barba, F. Harper, T. Harada, M. Kohara, S. Goulinet, Y. Matsuura, G. Eder, Z. Schaff, M.J. Chapman, T. Miyamura, C. Bréchot, Hepatitis C virus core protein shows a cytoplasmic localization and associates to cellular lipid storage droplets, Proc. Natl. Acad. Sci. U. S. A. 94 (1997) 1200–1205, https://doi.org/10.1073/pnas.94.4.1200.

[24] E.A. Monson, A.M. Trenerry, J.L. Laws, J.M. Mackenzie, K.J. Helbig, Lipid droplets and lipid mediators in viral infection and immunity, FEMS Microbiol. Rev. 45 (2021) fuaa066, https://doi.org/10.1093/femsre/fuaa066.

[25] M.R. Dent, I. López-Duarte, C.J. Dickson, N.D. Geoghegan, J.M. Cooper, I.R. Gould, R. Krams, J.A. Bull, N.J. Brooks, M.K. Kuimova, Imaging phase separation in model lipid membranes through the use of BODIPY based molecular rotors, Phys. Chem. Chem. Phys. 17 (2015) 18393–18402, https://doi.org/10.1039/c5cp01937k.

[26] M. Collot, S. Bou, T.K. Fam, L. Richert, Y. Mély, L. Danglot, A.S. Klymchenko, Probing polarity and heterogeneity of lipid droplets in live cells using a push-pull fluorophore, Anal. Chem. 91 (2019) 1928–1935, https://doi.org/10.1021/acs.analchem.8b04218.

[27] S.I. Suarez, C.C. Warner, H. Brown-Harding, A.M. Thooft, B. VanVeller, J. C. Lukesh, Highly selective staining and quantification of intracellular lipid droplets with a compact push-pull fluorophore based on benzothiadiazole, Org. Biomol. Chem. 18 (2020) 495–499, https://doi.org/10.1039/c9ob02486g.

[28] J. Yin, M. Peng, Y. Ma, R. Guo, W. Lin, Rational design of a lipid-droplet-polarity based fluorescent probe for potential cancer diagnosis, Chem. Commun. (Camb) 54 (2018) 12093–12096, https://doi.org/10.1039/c8cc07398h.

[29] K.-N. Wang, L.-Y. Liu, D. Mao, S. Xu, C.-P. Tan, Q. Cao, Z.-W. Mao, B. Liu, A polarity-sensitive ratiometric fluorescence probe for monitoring changes in lipid droplets and nucleus during ferroptosis, Angew. Chem. Int. Ed. Engl. 60 (2021) 15095–15100, https://doi.org/10.1002/anie.202104163.

[30] M. Collot, T.K. Fam, P. Ashokkumar, O. Faklaris, T. Galli, L. Danglot, A. S. Klymchenko, Ultrabright and fluorogenic probes for multicolor imaging and tracking of lipid droplets in cells and tissues, J. Am. Chem. Soc. 140 (2018) 5401–5411, https://doi.org/10.1021/jacs.7b12817.

[31] L. Guo, M. Tian, Z. Zhang, Q. Lu, Z. Liu, G. Niu, X. Yu, Simultaneous two-color visualization of lipid droplets and endoplasmic reticulum and their interplay by single fluorescent probes in lambda mode, J. Am. Chem. Soc. 143 (2021) 3169–3179, https://doi.org/10.1021/jacs.0c12323.

[32] M.-S. Zhu, X.-Q. Zhang, Y.-N. Wang, Y.-J. Xu, R. Sun, J.-F. Ge, Preparation of chromeno[b]quinoline derivatives and their application for lipid droplets markers, J. Org. Chem. 87 (2022) 10385–10389, https://doi.org/10.1021/acs.joc.2c00667.

[33] Y. Tatenaka, H. Kato, M. Ishiyama, K. Sasamoto, M. Shiga, H. Nishitoh, Y. Ueno, Monitoring lipid droplet dynamics in living cells by using fluorescent probes, Biochemistry 58 (2019) 499–503, https://doi.org/10.1021/acs.biochem.8b01071.

[34] P. Greenspan, E.P. Mayer, S.D. Fowler, Nile red: a selective fluorescent stain for intracellular lipid droplets, J. Cell Biol. 100 (1985) 965–973, https://doi.org/10.1083/jcb.100.3.965.

[35] J. Valanciunaite, E. Kempf, H. Seki, D.I. Danylchuk, N. Peyriéras, Y. Niko, A. S. Klymchenko, Polarity mapping of cells and embryos by improved fluorescent solvatochromic pyrene probe, Anal. Chem. 92 (2020) 6512–6520, https://doi.org/10.1021/acs.analchem.0c00023.

[36] Y. Niko, P. Didier, Y. Mely, G. Konishi, A.S. Klymchenko, Bright and photostable push-pull pyrene dye visualizes lipid order variation between plasma and intracellular membranes, Sci. Rep. 6 (2016) 18870, https://doi.org/10.1038/srep18870.

[37] H. Tian Jr., A.C. Sedgwick, H.-H. Han, S. Sen, G.-R. Chen, Y. Zang, J.L. Sessler, T. D. James, J. Li, X.-P. Fluorescent, Probes for the imaging of lipid droplets in live cells, Coord. Chem. Rev. 427 (2021) 213577, https://doi.org/10.1016/j.ccr.2020.213577.

[38] H. Zhu, J. Fan, J. Du, X. Peng, Fluorescent probes for sensing and imaging within specific cellular organelles, Acc. Chem. Res. 49 (2016) 2115–2126, https://doi.org/10.1021/acs.accounts.6b00292.

[39] S. Park, H. Otomo, L. Zheng, H. Sugiyama, Discerning the chemistry in individual organelles with small-molecule fluorescent probes, Angew. Chem. Int. Ed. Engl. 55 (2016) 13658–13699, https://doi.org/10.1002/anie.201510721.

[40] S. Park, H. Otomo, L. Zheng, H. Sugiyama, Highly emissive deoxyguanosine analogue capable of direct visualization of B-Z transition, Chem. Commun. (Camb) 50 (2014) 1573–1575, https://doi.org/10.1039/c3cc48297a.

[41] I. Okamura, S. Park, R. Hiraga, S. Yamamoto, H. Sugiyama, Synthesis, photophysical properties, and enzymatic incorporation of an emissive thymidine analogue, Chem. Lett. 46 (2017) 245–248, https://doi.org/10.1246/cl.161024.

[42] S. Hirashima, J.H. Han, H. Tsuno, Y. Tanigaki, S. Park, H. Sugiyama, New size-expanded fluorescent thymine analogue: synthesis, characterization, and application, Chemistry 25 (2019) 9913–9919, https://doi.org/10.1002/chem.201900843.

[43] W.A. Wee, J.H. Yum, S. Hirashima, H. Sugiyama, S. Park, Synthesis and application of a 19F-labeled fluorescent nucleoside as a dual-mode probe for i-motif DNAs, RSC Chem. Biol. 2 (2021) 876–882, https://doi.org/10.1039/d1cb00020a.

[44] T. Kumagai, B. Kinoshita, S. Hirashima, H. Sugiyama, S. Park, Thiophene-extended fluorescent nucleosides as molecular rotor-type fluorogenic sensors for biomolecular interactions, ACS Sens. 8 (2023) 923–932, https://doi.org/10.1021/acssensors.2c02617.

[45] W. Zhang, L. Xu, L. Zhu, Y. Liu, S. Yang, M. Zhao, Lipid droplets, the central hub integrating cell metabolism and the immune system, Front. Physiol. 12 (2021) 746749, https://doi.org/10.3389/fphys.2021.746749.

[46] D.M. Boucher, V. Vijithakumar, M. Ouimet, Lipid droplets as regulators of metabolism and immunity, Immunometabolism 3 (2021) e210021, https://doi.org/10.20900/immunometab20210021.

[47] J. Marschallinger, T. Iram, M. Zardeneta, S.E. Lee, B. Lehallier, M.S. Haney, J. V. Pluvinage, V. Mathur, O. Hahn, D.W. Morgens, J. Kim, J. Tevini, T.K. Felder, H. Wolinski, C.R. Bertozzi, M.C. Bassik, L. Aigner, T. Wyss-Coray, Lipid-droplet-accumulating microglia represent a dysfunctional and proinflammatory state in the aging brain, Nat. Neurosci. 23 (2020) 194–208, https://doi.org/10.1038/s41593-019-0566-1.

[48] J. Zhang, Y. Lan, S. Sanyal, Modulation of lipid droplet metabolism-a potential target for therapeutic intervention in Flaviviridae infections, Front. Microbiol. 8 (2017) 2286, https://doi.org/10.3389/fmicb.2017.02286.

[49] E.A. Monson, K.M. Crosse, M. Duan, W. Chen, R.D. O'Shea, L.M. Wakim, J.M. Carr, D.R. Whelan, K.J. Helbig, Intracellular lipid droplet accumulation occurs early

following viral infection and is required for an efficient interferon response, Nat. Commun. 12 (2021) 4303, https://doi.org/10.1038/s41467-021-24632-5.
[50] L. Mendive-Tapia, M. Vendrell, Activatable fluorophores for imaging immune cell function, Acc. Chem. Res. 55 (2022) 1183–1193, https://doi.org/10.1021/acs.accounts.2c00070.
[51] A.H. Ashoka, P. Ashokkumar, Y.P. Kovtun, A.S. Klymchenko, Solvatochromic near-infrared probe for polarity mapping of biomembranes and lipid droplets in cells under stress, J. Phys. Chem. Lett. 10 (2019) 2414–2421, https://doi.org/10.1021/acs.jpclett.9b00668.
[52] D.I. Danylchuk, P.-H. Jouard, A.S. Klymchenko, Targeted aolvatochromic fluorescent probes for imaging lipid order in organelles under oxidative and mechanical stress, J. Am. Chem. Soc. 143 (2021) 912–924, https://doi.org/10.1021/jacs.0c10972.
[53] M. Kono, Y. Takagi, S. Kawauchi, A. Wada, T. Morikawa, K. Funakoshi, Non-activated T and B lymphocytes become morphologically distinguishable after detergent treatment, Cytometry A 83 (2013) 396–402, https://doi.org/10.1002/cyto.a.22262, 83.
[54] D.A. Clark, E.L. Foulds Jr., F.H. Wilson Jr., Effects of hydrogen peroxide on lipoproteins and associated lipids, Lipids 4 (1969) 1–8, https://doi.org/10.1007/BF02531786.
[55] S. Kersten, The impact of fasting on adipose tissue metabolism, Biochim. Biophys. Acta Mol. Cell Biol. Lipids 1868 (2023) 159262, https://doi.org/10.1016/j.bbalip.2022.159262.
[56] K. Simons, E. Ikonen, How cells handle cholesterol, Science 290 (2000) 1721–1726, https://doi.org/10.1126/science.290.5497.1721.
[57] E. Ikonen, Cellular cholesterol trafficking and compartmentalization, Nat. Rev. Mol. Cell Biol. 9 (2008) 125–138, https://doi.org/10.1038/nrm2336.
[58] R. Onodera, K. Motoyama, A. Okamatsu, T. Higashi, R. Kariya, S. Okada, H. Arima, Involvement of cholesterol depletion from lipid rafts in apoptosis induced by methyl-β-cyclodextrin, Int. J. Pharm. 452 (2013) 116–123, https://doi.org/10.1016/j.ijpharm.2013.04.071.
[59] S. Oncul, A.S. Klymchenko, O.A. Kucherak, A.P. Demchenko, S. Martin, M. Dontenwill, Y. Arntz, P. Didier, G. Duportail, Y. Mély, Liquid ordered phase in cell membranes evidenced by a hydration-sensitive probe: effects of cholesterol depletion and apoptosis, Biochim. Biophys. Acta 1798 (2010) 1436–1443, https://doi.org/10.1016/j.bbamem.2010.01.013.
[60] O.A. Kucherak, S. Oncul, Z. Darwich, D.A. Yushchenko, Y. Arntz, P. Didier, Y. Mély, A.S. Klymchenko, Switchable nile red-based probe for cholesterol and lipid order at the outer leaflet of biomembranes, J. Am. Chem. Soc. 132 (2010) 4907–4916, https://doi.org/10.1021/ja100351w.
[61] D. Lumaquin, E. Johns, E. Montal, J.M. Weiss, D. Ola, A. Abuhashem, R.M. White, An in vivo reporter for tracking lipid droplet dynamics in transparent zebrafish, Elife 10 (2021) e64744, https://doi.org/10.7554/eLife.64744.
[62] V.H. Quinlivan, S.A. Farber, Lipid uptake, metabolism, and transport in the larval zebrafish, Front. Endocrinol. 8 (2017) 319, https://doi.org/10.3389/fendo.2017.00319.
[63] J.D. Carten, M.K. Bradford, S.A. Farber, Visualizing digestive organ morphology and function using differential fatty acid metabolism in live zebrafish, Dev. Biol. 360 (2011) 276–285, https://doi.org/10.1016/j.ydbio.2011.09.010.
[64] M. Ishigaki, T. Nishii, P. Puangchit, Y. Yasui, C.W. Huck, Y. Ozaki, Noninvasive, high-speed, near-infrared imaging of the biomolecular distribution and molecular mechanism of embryonic development in fertilized fish eggs, J. Biophot. 11 (2018) e201700115, https://doi.org/10.1002/jbio.201700115.
[65] E. Bik, M. Ishigaki, A. Blat, A. Jasztal, Y. Ozaki, K. Malek, M. Baranska, Lipid droplet composition varies based on medaka fish eggs development as revealed by NIR-, MIR-, and raman imaging, Molecules 25 (2020) 817, https://doi.org/10.3390/molecules25040817.
[66] J. Valanciunaite, E. Kempf, H. Seki, E.I. Danylchuk, N. Peyriéras, Y. Niko, A. S. Klymchenko, Polarity mapping of cells and embryos by improved fluorescent solvatochromic pyrene probe, Anal. Chem. 92 (2020) 6512–6520, https://doi.org/10.1021/acs.analchem.0c00023.
[67] A.H. Ashoka, P. Ashokkumar, Y.P. Kovtun, A.S. Klymchenko, Solvatochromic near-infrared probe for polarity mapping of biomembranes and lipid droplets in cells under stress, J. Phys. Chem. Lett. 10 (2019) 2414–2421, https://doi.org/10.1021/acs.jpclett.9b00668.
[68] M. Zajac, P. Hrobárik, P. Magdolen, P. Foltínová, P. Zahradník, Donor–π-acceptor benzothiazole-derived dyes with an extended heteroaryl-containing conjugated system: synthesis, DFT study and antimicrobial activity, Tetrahedron 64 (2008) 10605–10618, https://doi.org/10.1016/j.tet.2008.08.064.
[69] J. Jose, J.K. Burgess, Syntheses and properties of water-soluble Nile Red derivatives, J. Org. Chem. 71 (2006) 7835–7839, https://doi.org/10.1021/jo061369v.
[70] A.A. Pakhomov, I.E. Deyev, N.M. Ratnikova, S.P. Chumakov, V.B. Mironiuk, Y. N. Kononevich, A.M. Muzafarov, V.I. Martynov, BODIPY-based dye for no-wash live-cell staining and imaging, Biotechniques 63 (2017) 77–80, https://doi.org/10.2144/000114577.
[71] N. Aknine, A.S. Klymchenko, Push−Pull fluorescent dyes with trifluoroacetyl acceptor for High- fidelity sensing of polarity and heterogeneity of lipid droplets, Anal. Chem. 96 (2024) 13242–13251, https://doi.org/10.1021/acs.analchem.4c02322.
[72] D.T. Dinh, C.-Y. Li, M.-W. Wu, C.-F. Hsieh, X.-Y. Chen, C.-C. Chang, An acridone based fluorescent dye for lipid droplet tracking and cancer diagnosis, J. Photochem. Photobiol., B 258 (2024) 113999, https://doi.org/10.1016/j.jphotobiol.2024.113000.
[73] Q. Wang, D. Li, Z. Zhang, L. Shen, H. Xu, Z. Wang, C. Redshawd, Q. Zhang, Polarity-Sensitive fluorescent probes based on triphenylamine for fluorescence lifetime imaging of lipid droplets, Spectrochim. Acta Mol. Biomol. Spectrosc. 330 (2025) 125694, https://doi.org/10.1016/j.saa.2024.125694.
[74] Y.-H. Yang, W.-L. Cui, M.-H. Wang, J.-Y. Wang, Synthesis of fluorescent dyes based on the electron-withdrawing core of malononitrile and construction of viscosity-sensitive AIE probe with large Stokes shift for lipid droplets imaging, Dyes Pgm 233 (2025) 112528, https://doi.org/10.1016/j.dyepig.2024.112528.